JOURNAL OF COMPUTATIONAL PHYSICS **136,** 411–424 (1997)
ARTICLE NO. CP975764

Multigrid Computation of Stratified Flow over Two-Dimensional Obstacles

M. F. Paisley

Department of Mathematics and Statistics, School of Computing, Staffordshire University, Stafford, United Kingdom ST18 0AD
E-mail: cmtmfp@soc.staffs.ac.uk

Received December 3, 1996; accepted June 11, 1997

A robust multigrid method for the incompressible Navier–Stokes equations is presented and applied to the computation of viscous flow over obstacles in a bounded domain under conditions of neutral stability and stable density stratification. Two obstacle shapes have been used, namely a vertical barrier, for which the grid is Cartesian, and a smooth cosine-shaped obstacle, for which a boundary-conforming transformation is incorporated. Results are given for laminar flows at low Reynolds numbers and turbulent flows at a high Reynolds number, when a simple mixing length turbulence model is included. The multigrid algorithm is used to compute steady flows for each obstacle at low and high Reynolds numbers in conditions of weak static stability, defined by $K = ND/\pi U \leq 1$, where U, N, and D are the upstream velocity, bouyancy frequency, and domain height respectively. Results are also presented for the vertical barrier at low and high Reynolds number in conditions of strong static stability, $K > 1$, when lee wave motions ensure that the flow is unsteady, and the multigrid algorithm is used to compute the flow at each timestep.

1. INTRODUCTION

Multigrid methods are becoming an indispensable part of numerical procedures in many fields of application. The achievement of the goal of grid-independent convergence rates allows the possibility of high resolution computations being performed in computing times that are realistic and affordable. Fundamental concepts tended to be demonstrated in early work using the benchmark problem of a recirculating homogeneous steady laminar flow in a driven cavity with simple Dirichlet boundary conditions and discretized on a square Cartesian grid. Multigrid methods have since been applied much more widely to more general flows containing features such as inhomogeneity, Neumann boundary conditions, and discretized on nonuniform and/or curvilinear grids and requiring turbulence modeling.

This paper reports an investigation of the application of multigrid methods to the computation of density-stratified flow over obstacles. Such flows are of immediate relevance to atmospheric flow over terrain, and provide insight into activities such as local and mesoscale meteorology and the prediction of dispersion of atmospheric contaminants. A fundamental characteristic of the flow of a stratified fluid over an obstacle is the production of lee waves, which can persist for long distances downstream, making the use of stretched grids unavoidable. When lee wave amplitudes are large, wave-breaking can occur, and under these circumstances streamline reversal leads to a local region of statically unstable flow where mixing occurs. Adequate modeling of such processes, as well as lee-side separation, requires the use of viscous equations with, preferably, a high Reynolds number and the use of a turbulence model. When lee waves are present, wave propagation (upstream as well as downstream) means that time dependence should also be included. The range of phenomena is thus wide in two dimensions, and even wider in three, with additional questions concerning the passage of fluid over or around isolated obstacles. Such flows present a challenge to the techniques of computational fluid dynamics, and computing times for single grid solution algorithms for the incompressible Navier–Stokes equations are exceedingly long, due to the ineffectiveness of standard iterative methods at smoothing low frequency components of the solution errors. The multigrid technique represents errors on a hierarchy of successively coarser grids, rendering each frequency band high relative to an appropriately coarse grid and amenable to effective smoothing, leading to rapid convergence rates. The objective of the work described here is an investigation of the effectiveness of the multigrid applied to the computation of steady two-dimensional flow over an obstacle, for neutral or stably-stratified conditions, for Cartesian or non-Cartesian geometry, and for laminar or turbulent flow, and to provide pointers for dealing with flows which are unsteady.

Smoothing algorithms proposed to solve the discrete Navier–Stokes equations are divided into two main categories, namely decoupled and coupled. Decoupled methods employ relaxation of each equation over the whole domain, and cycle through the equations in turn to achieve the coupling between variables. Pressure correction methods are of this type, the most popular of which are variants of the SIMPLE (semi-implicit method for pressure-linked equations; Patankar [1]) algorithm. The suitability of the

0021-9991/97 $25.00

SIMPLE algorithm as a smoother for the multigrid has been analysed by Shaw & Sivaloganathan [2] and has been demonstrated for a variety of test cases by Sivaloganathan and Shaw [3] and Lien and Leschziner [4, 5], for example. Coupled methods, on the other hand, solve a locally coupled set of discrete equations followed by relaxation over the whole domain, of which the SCGS (symmetric coupled Gauss–Seidel; Vanka [6]) algorithm is probably the best known. Analysis [7] suggests that the smoothing rates for SCGS are better than for SIMPLE for low Reynolds numbers, although for higher Reynolds numbers the issue is unclear. Numerical experiments in [7] with the driven cavity problem confirmed this, with little to choose between the two approaches for the highest Reynolds number on the finest grid used. Other numerical results [8] suggest that SCGS is superior, but only when implemented in lines, not pointwise, if cell aspect ratios are large. Both approaches are in wide use, however, and, in the absence of a clear consensus, the smoothing algorithm chosen here is SIMPLE. A variant of SIMPLE was already implemented in single-grid form and was thus the convenient choice. This has the side effect that comparisons of computing times between a single grid and a multigrid are readily available. Coupled algorithms are poor as single-grid smoothers and are not generally implemented in single-grid codes, so such speed-up factors are generally meaningless.

The trends expected in the results are clear from the outset: the effectiveness of the multigrid depends on the measure of ellipticity in the discrete equations, which, for the steady Navier–Stokes equations, diminishes with increasing Reynolds number. As the Reynolds number increases, multigrid performance in terms of residual reduction per cycle is expected to decrease. In the case of an unsteady flow, although special multigrid procedures have been developed for parabolic problems ([9], for example), we adopt the common practice (see [10]) of regarding the time development as a series of steady solutions at successive time steps, with each being the initial condition for finding the next. In this case what is sought at each timestep is a set of small changes which are of high frequency. The multigrid in this case may be expected to be less effective than for a steady flow, for most of the low-frequency information (the underlying flow structure) is already known and cycling over coarse grids will be of little avail. Multigrid performance, when compared to single grid performance, is thus expected to be poorer in the individual timesteps of an unsteady computation than in a steady computation.

The organization of the paper is as follows: Section 2 describes the details of the mathematical model, the computational domain, and boundary conditions, and the turbulence model used for the high Reynolds number cases. Section 3 describes the numerical method used on the finest grid of any nested set while the implementation of the multigrid is given in Section 4. The numerical results are discussed in Section 5 with an interpretation of the steady and unsteady flows obtained. The paper ends with some conclusions and directions for future work in Section 6.

2. MATHEMATICAL MODEL

Equations of Motion

Under the Boussinesq approximation, in which density variations are neglected in the advection terms in the momentum equations, the equations of motion describing two-dimensional turbulent stratified flow are

$$\frac{Du_i}{Dt} = -\frac{\partial p}{\partial x_i} - \frac{1}{F_h^2}\,\vartheta\hat{z} + \frac{\partial}{\partial x_j}\left\{\frac{1}{\mathrm{Re}}\frac{\partial u_i}{\partial x_j} + \tau_{ij}\right\} \tag{1}$$

$$\frac{\partial u_i}{\partial x_i} = 0 \tag{2}$$

$$\frac{D\vartheta}{Dt} = \frac{\partial}{\partial x_j}\left\{\frac{1}{\mathrm{Re}\cdot\mathrm{Pr}}\frac{\partial \vartheta}{\partial x_j} + H_j\right\}. \tag{3}$$

Equations (1)–(3) respectively express conservation of momentum in the two coordinate directions, the incompressibility constraint, and the transport of the scalar variable responsible for changes in density. F_h is the Froude number, given by $F_h = U/\mathrm{Nh}$, where U is the freestream velocity, h the obstacle height, and N the bouyancy frequency (constant for a linear density gradient). ϑ is the density scalar given by $\vartheta = D(\rho - \rho_o)/\Delta\rho$, where ρ is the physical density and $\Delta\rho$ the magnitude of the density change over the nondimensional domain height D. $\hat{z}$ is the unit vector in the vertical direction and Pr is the turbulent Prandtl number. τ_{ij} is the Reynolds stress tensor and H_j the turbulent buoyancy flux, both of which are defined later. For laminar flows Pr is replaced with the Schmidt number Sc, taken to be 1000. The equations have been nondimensionalized by U, h, and the reference density ρ_o.

Domain and Boundary Conditions

The computational domain and boundary conditions considered in this paper are illustrated in Fig. 1 and are intended to mimic experimental apparatus where an obstacle is towed through a water tank, see Castro *et al.* [11]. The geometry for such an experiment would usually be inverted. Uniform horizontal velocity and a linear density profile are specified at inflow, while simple zero gradient conditions are applied for all variables at outflow. A ''moving wall'' condition is applied at the top of the domain and corresponds to the bottom of the towing tank. Two obstacle shapes have been used: a vertical barrier, for which the

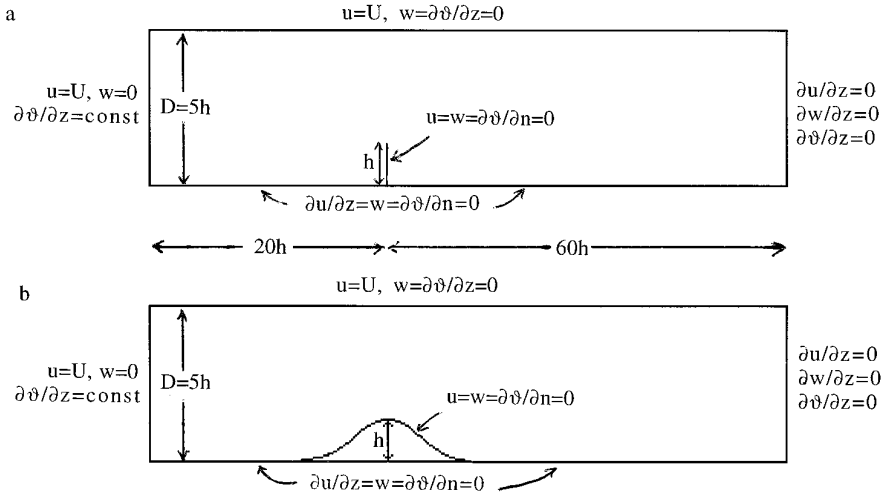

FIG. 1. Computational domain and boundary conditions for flow over (a) the vertical barrier and (b) the cosine hill.

computational grid is Cartesian, and an obstacle with smooth profile given by $h(x) = 0.5(1 + \cos(\pi x/1.8))$ for which the grid is curvilinear. Obstacles of both these kinds have been used in experimental studies [11] and previous computational work [12–14]. No-slip boundary conditions are applied to the obstacle, and zero stress conditions upstream and downstream, mimicking a free surface. In the case of the cosine-shaped obstacle, no-slip conditions are applied for $|x| \le 8$, modeling the geometry of an obstacle mounted on a base plate. The initial condition for all computations is that of uniform horizontal velocity, and, in the case of the unsteady computations, this corresponds to an "impulsive start."

Turbulence Model

Convergence rates for multigrid methods tend to deteriorate with increasing Reynolds number, and especially so when complex turbulence modeling is introduced; see Lien and Leschziner [4, 5]. Here we use a simple mixing length eddy viscosity model, where the components of the Reynolds stress tensor and the turbulent buoyancy flux are given as

$$\tau_{ij} = \nu_t \left\{ \frac{\partial u_i}{\partial x_j} + \frac{\partial u_j}{\partial x_i} \right\}, \qquad H_j = (\nu_t/\mathrm{Pr}) \frac{\partial \vartheta}{\partial x_j},$$

where Pr is taken to be 0.9. The eddy viscosity is determined as $\nu_t = l^2 \mathrm{S}$, where the strain rate S is given by

$$S^2 = \frac{1}{2} \left\{ \frac{\partial u_i}{\partial x_j} + \frac{\partial u_j}{\partial x_i} \right\}^2,$$

and the mixing length is specified by the commonly used relation $1/l = 1/l_o + 1/\kappa z$, which limits the rise in mixing length (to a constant, l_o). Here κ is von Karman's constant and z is the distance from the nearest solid surface.

In stratified flow the eddy viscosity may be modified according to the local conditions of stability. All indications suggest that vertical fluctuations are damped out in the presence of a stable density gradient, while they are magnified once the gradient reverses, as in a recirculation region or breaking lee wave. Defining the value of the local gradient Richardson number as

$$\mathrm{Ri} = \frac{1}{F_h^2} \frac{\partial \vartheta/\partial z}{S^2}$$

and setting a level for the critical value, $\mathrm{Ri_c}$, below which turbulence cannot be sustained, the eddy viscosity becomes (see Mason and Sykes [15]):

$$\text{Stable } (\mathrm{Ri} > 0): \quad \begin{cases} \nu_t (1 - \mathrm{Ri}/\mathrm{Ri_c})^2, & 0 \le \mathrm{Ri} \le \mathrm{Ri_c} \\ 0, & \mathrm{Ri_c} \le \mathrm{Ri} \end{cases} \tag{4}$$

$$\text{Unstable } (\mathrm{Ri} < 0): \quad \nu_t (1 - \mathrm{Ri})^{1/2}. \tag{5}$$

This formulation is equivalent to a modification of the mixing length. Choosing a small value for $\mathrm{Ri_c}$ (say unity or less) means that the viscosity in the flow outside the neighbourhood of shear layers and recirculation zones has no contribution from the turbulent eddy viscosity and the flow is effectively laminar.

3. NUMERICAL MODEL

Discretization

Equations (1) and (3) are often expressed in the form

of the two-dimensional convection-diffusion equation with source term

$$\frac{\partial \phi}{\partial t} + \frac{\partial}{\partial x}(u\phi) + \frac{\partial}{\partial z}(w\phi) = \frac{\partial}{\partial x}\left(\Gamma \frac{\partial \phi}{\partial x}\right) + \frac{\partial}{\partial z}\left(\Gamma \frac{\partial \phi}{\partial z}\right) + S, \tag{6}$$

where ϕ may stand for u, w, or ϑ. The finite volume approach to approximating (6) is to integrate over a control volume, of area ΔV and apply the divergence theorem. In the case of a rectangular Cartesian grid, this gives

$$\frac{\partial \phi}{\partial t}\Delta V + \sum \left[\left(u\phi - \Gamma \frac{\partial \phi}{\partial x} \right) \Delta z - \left(w\phi - \Gamma \frac{\partial \phi}{\partial z} \right) \Delta x \right] = S\,\Delta V, \tag{7}$$

where the summation is taken over the four sides of the control volume. In this work, Eq. (7) is discretized on a staggered grid with the usual arrangement of variables and associated control volumes, Fig. 2, and the problem reduces to that of providing estimates of flow quantities on cell sides. Local interpolation is used for u, w, and Γ (Γ is constant for laminar flows), and the diffusive terms are obtained by standard two-point differencing. The advective terms, on the other hand, are dealt with using a second-order flux-limited scheme designed to prevent spurious oscillation, originally developed for unsteady inviscid compressible flows (Van Leer [16]) and adapted as follows (Leonard and Mokhtari [17]).

Considering the flow across cell boundaries to be one-dimensional in directions normal to the cell faces, let ϕ_p be the value of the flow variable (u, w, or ϑ) at the centre of the cell under consideration, with ϕ_u and ϕ_d the corresponding values at the centres of the cells immediately upwind and downwind respectively. The procedure for obtaining the estimate on the downwind cell face, ϕ_f, midway between ϕ_p and ϕ_d is based on calculating the ratio of differences

$$\hat{\phi}_p = \frac{\phi_p - \phi_u}{\phi_d - \phi_u}.$$

Values of $\hat{\phi}_p$ in the range $0 \le \hat{\phi}_p \le 1$ correspond to a monotonic variation of ϕ over the three cells, and a variety of schemes can be proposed which preserve this property (see [17]). One of the simplest is to take the harmonic mean of the values given by averaging neighbouring values (central differencing) and second-order upwind interpolation, that is,

$$\phi_f = \frac{1}{2}(\phi_p + \phi_d)\hat{\phi}_p + \frac{1}{2}(3\phi_p - \phi_u)(1 - \hat{\phi}_p).$$

This is more conveniently expressed as

$$\phi_f = \phi_p + (\phi_d - \phi_p)\hat{\phi}_p,$$

where the estimate now consists of the value immediately upstream (first-order upwinding) plus a second-order flux-limited correction. Values of $\hat{\phi}_p$ outside the range $0 \le \hat{\phi}_p \le 1$ correspond to extreme points in the flow, and only the value immediately upstream is used. The effectiveness of this scheme is demonstrated in [13], where monotonic density profiles obtained are contrasted with those containing unphysical overshoot arising from the use of a non-monotonic scheme.

Collecting the convective and diffusive contributions from the four cell faces in this manner allows the steady part of Eq. (7) to be expressed in the form

$$a_p \phi_p = \sum a_m \phi_m + S_p^{\phi}, \tag{8}$$

where the summation is taken over the values at the centres of the four neighboring cells, and the multiplying coefficients contain the convective and diffusive flow rates. The source term includes the second-order corrections from the convective scheme just described. Expression (8) is an implicit equation for the steady state solution, and comprises a diagonally dominant set for each of the variables u, w, and ϑ which is solved using the ADI method and a standard tridiagonal matrix algorithm.

For unsteady flows, the time derivative in (7) is discretised using a second-order backward difference, namely,

$$\frac{3\phi_p^{n+1} - 4\phi_p^n + \phi_p^{n-1}}{2\Delta t},$$

and Eq. (8) can now be regarded as an implicit equation for the solution at the new time level $(n+1)$, with simple modifications to the diagonal coefficients and the source term,

$$\left(a_p + \frac{3\Delta V}{2\Delta t}\right)\phi_p^{n+1} = \sum a_m \phi_m^{n+1} + \left(S_p^{\phi} + \frac{4\phi_p^n - \phi_p^{n-1}}{2\Delta t}\right). \tag{9}$$

As far as the meshing arrangements are concerned, for the flows over the vertical barrier a Cartesian grid was used,

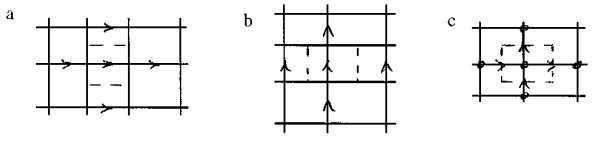

FIG. 2. Control volumes for staggered grid arrangement of (a) u velocity, (b) w velocity, and (c) continuity and density.

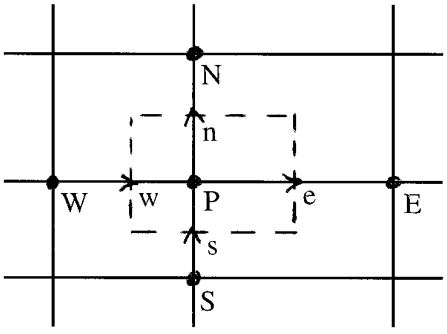

FIG. 3. Fine grid continuity control volume and associated variables for fine grid pressure correction step.

with the location of the barrier coinciding with a vertical line of horizontal velocities. These velocities are forced to zero by suitable modification of source terms, and neighbouring equation coefficients are modified appropriately. For flows over smooth geometry, however, a simple transformation was used to stretch the vertical coordinates. This introduces a volume scale factor and other metric terms into the momentum and scalar transport equations, and additional source terms arising from the curvilinear coordinate derivatives. Many of the computational details can be found in Apsley [18].

SIMPLE Smoothing Algorithm

Following updates to the velocities via the solution of the discrete momentum equations, the SIMPLE algorithm [1] employs relationships between corrections to velocities and adjacent pressures of the form (see Fig. 3)

$$u'_w = \frac{A_w}{a_w}(p'_W - p'_P) \qquad \text{and} \qquad w'_s = \frac{A_s}{a_s}(p'_S - p'_P), \quad (10)$$

where u', w', and p' are the corrections to be added to the current solution u^*, w^*, and p^*. Use is then made of the discrete continuity equation written in terms of velocity corrections

$$(u'_e - u'_w)\Delta z + (w'_n - w'_s)\Delta x = -R^c, \quad (11)$$

where R^c is the continuity residual (mass imbalance) of the current solution. Substituting (10) and the corresponding relations for u'_e and w'_n into (11) gives a Poisson-type equation for the pressure corrections

$$a_P p'_P - \sum a_M p'_M = -R^c. \quad (12)$$

Equation (12) is solved using four ADI sweeps to yield the pressure corrections, which are used to update the velocities through relationships (10).

In the case of stratified flows the additional transport equation for the density field is now solved

$$a_P \vartheta_P = \sum a_M \vartheta_M + S_P^\vartheta, \quad (13)$$

and this completes one outer iteration. The process is not convergent without some form of underrelaxation, the exact values for which are problem dependent. Typical values for the momentum equations were in the range 0.4–0.8, while 0.8–0.95 suffices for the scalar transport equation. The value used for the addition of the pressure corrections was in the range 0.25–0.4.

4. MULTIGRID IMPLEMENTATION

Coarse Grid Equations

It is well known that for linear operators the appropriate multigrid procedure is the Correction Scheme (CS), whereas for nonlinear operators it is the Full Approximation Scheme (FAS)—see Brandt [19], for example. In the former, only corrections need be calculated on coarse grids, while in the latter, the computation of changes in the solution requires the storage of the full restricted solution. The Navier–Stokes equations are nonlinear in velocity but linear in pressure, so a mixture of FAS and CS may be used. Denoting the linear and nonlinear discrete operators on the fine grid to be L_h and N_h respectively, the discrete horizontal momentum equation can be written symbolically as

$$N_h u_h + L_h p_h = 0. \quad (14)$$

Suppose our current approximations to the exact horizontal velocity u_h and pressure p_h are $\tilde{u}_h$ and $\tilde{p}_h$ respectively. These satisfy Eq. (14) to the extent of a residual $\tilde{R}_h$,

$$N_h \tilde{u}_h + L_h \tilde{p}_h = \tilde{R}_h. \quad (15)$$

Subtraction of (15) from (14) yields the relationship

$$N_h u_h = N_h \tilde{u}_h - L_h p'_h - \tilde{R}_h, \quad (16)$$

where $p'_h = p_h - \tilde{p}_h$. Relationship (16) is the basis of the coarse grid equations. To obtain the coarse grid form of this equation a restriction operator I_h^{2h} is defined (see later) to transfer the velocities and the residuals to the coarse grid. The coarse grid equation thus takes the form

$$N_{2h} u_{2h} = N_{2h} I_h^{2h} \tilde{u}_h - L_{2h} p'_{2h} - I_h^{2h} \tilde{R}_h. \quad (17)$$

Starting from the initial conditions $u_{2h} = I_h^{2h}\tilde{u}_h$ and $p'_{2h} = 0$, a coarse grid pressure correction step is now used to yield the new coarse grid velocities u_{2h} and the coarse grid pressure corrections p'_{2h}. Given a prolongation operator I_{2h}^h the changes in the coarse grid velocities and the pressure corrections are then transferred back to the fine grid and the fine grid solution updated as follows:

$$u_h = \tilde{u}_h + I_{2h}^h(u_{2h} - I_h^{2h}\tilde{u}_h) \qquad p_h = \tilde{p}_h + I_{2h}^h p'_{2h}. \quad (18)$$

Convergence on the fine grid implies that the residual forcing term in (17) is zero, and the equation is satisfied by $u_{2h} = I_h^{2h}\tilde{u}_h$ and $p'_{2h} = 0$, in which case the calculated changes are zero and interpolation leaves the fine grid solution unchanged.

Following the definition of the coarse grid equivalents of relations (10), the SIMPLE iteration on the coarse grid proceeds in a manner similar to the implementation on the fine grid described in the previous section. The procedure needs modification to allow the use of curvilinear grids, however. Denoting the discrete continuity operator on the fine grid to be C_h and rewriting expression (11) gives

$$C_h u_h = C_h \tilde{u}_h - R_h^c, \quad (19)$$

where, for convenience, $\tilde{u}$ is used as the current approximation, rather than u^*.

On a coarse grid this becomes

$$C_{2h}u_{2h} = C_{2h}I_h^{2h}\tilde{u}_h - I_h^{2h}R_h^c, \quad (20)$$

which is satisfied by the latest coarse grid approximation u^*_{2h} up to a residual R^c_{2h},

$$C_{2h}u^*_{2h} = C_{2h}I_h^{2h}\tilde{u}_h - I_h^{2h}R_h^c + R^c_{2h}. \quad (21)$$

The correction equation for coarse grids corresponding to (11) is obtained by subtracting (21) from (20), leaving

$$C_{2h}u'_{2h} = -R^c_{2h}. \quad (22)$$

This is identical in form to (11) and differs only in the definition of the right-hand side, which, from (21), is given by:

$$R^c_{2h} = C_{2h}u^*_{2h} - C_{2h}I_h^{2h}\tilde{u}_h + I_h^{2h}R_h^c. \quad (23)$$

When Cartesian grids are used, the restriction operator preserves mass fluxes (see next section), so that the last two terms in (23) cancel, leaving the first term only. When grids are curvilinear, however, mass fluxes are not preserved, and all three terms must be evaluated. When convergence is achieved on the fine grid (the last term is zero), no changes result from the coarse grid momentum equations, leaving the continuity residuals unchanged from their values calculated after restriction, and hence a zero right-hand side as required.

Substitution of the equivalent relationships to those of (10) into Eq. (22) yields an equation for corrections to pressure corrections

$$a_P p''_P - \sum a_M p''_M = -R^c_{2h}. \quad (24)$$

This is then solved and the velocities and pressure corrections updated to complete the coarse-grid pressure-correction step.

Following the pressure correction step the coarse grid density equation can now be solved. Under-relaxation was required for the coarse grid iteration and used the same values specified for the fine grid.

Grid Coarsening, Restriction, Prolongation, and Cycling

Coarse grids are generated in a manner which ensures that a coarse grid continuity cell is the sum of four fine grid cells, as in [3]. Restriction of residuals is carried out by summation, with appropriate scaling to preserve integrals. The restriction operator for flow variables, on the other hand, is based on taking the mean of nearest neighbouring values, as is commonly used in other implementations on staggered grids [3, 6]. For the coarse grid velocities this amounts to taking the mean of the two nearest neighbors, while for coarse grid pressures the mean of four nearest neighbors is taken; see Fig. 4. When grids are nonuniform

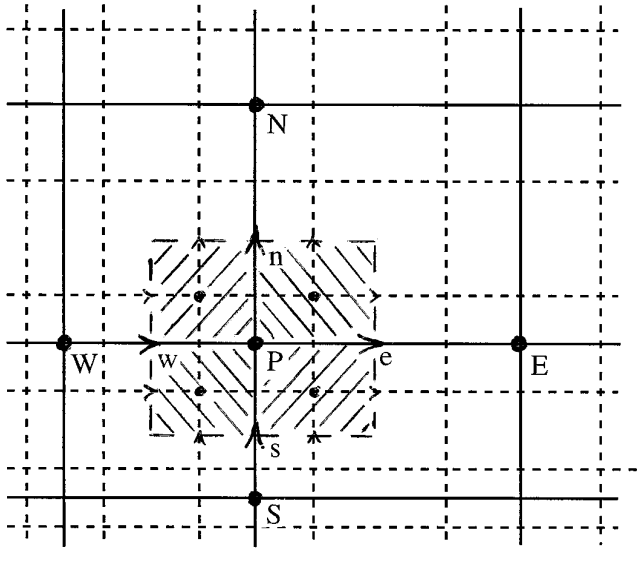

FIG. 4. Coarse grid continuity control volume (composed of four fine grid continuity control volumes, shown shaded) and associated variables for coarse grid pressure correction step.

the velocity means are weighted according to the lengths of the sides of fine-grid continuity cells. This has the effect of preserving mass fluxes for stretched Cartesian grids, so that a coarse grid continuity residual is the sum of the four corresponding continuity residuals on the fine grid (leading to the cancellation of the last two terms in (23)). For any grid, care must be taken over the implementation of velocity boundary conditions on coarse grids, for example at outflow, to ensure that continuity is maintained.

Following the iterations on the coarse grid, the changes to the velocity field and the pressure corrections are prolongated to the fine grid using standard bilinear interpolation. For the stratified flows it was found that, although the underlying discretisation guarantees monotonicity, destabilising (and unphysical) negative densities could be generated on the fine grid as a result of the interpolation of density changes. This was prevented by a simple modification as follows:

$$\vartheta_h = \mathrm{Max}[\tilde{\vartheta}_h + I_h^{2h}(\vartheta_{2h} - I_h^{2h}\tilde{\vartheta}_h), 0].$$

This was only necessary in the first two or three cycles when density changes from the coarse grids can be large, for tests showed that removing it thereafter had little effect. According to analysis [2] and numerical experiments [3], the smoothing rate (residual reduction per cycle) of the SIMPLE algorithm is always greater than 0.5 and in such cases Brandt's [19] recommendation is the use of *W* cycles over *V* cycles (see [19] for definitions). For almost all the computations described here it was found that *W* cycles were more effective than *V* cycles. This was certainly true for all the steady computations, the only exceptions being some of the unsteady computations on coarse grids.

5. RESULTS

Initial test runs with the multigrid method described above were made using the standard test problem of homogeneous recirculating flow in a driven cavity. The finest grid used contained 128×128 cells, from which four other grids are defined, the coarsest containing 8×8 cells. Although the code runs successfully with the coarsest grid containing 4×4 cells, and even 2×2, the computing times were marginally longer, presumably because the overheads associated with the grid transfers outweigh the efficiency savings of computing on the yet coarser grid. Fixed *W*-cycles were used, starting from zero initial conditions. Each multigrid cycle contained one presmoothing iteration, one postsmoothing iteration and up to ten iterations to solve the equations on the coarsest grid. Convergence was monitored using sums of absolute values of residuals over the whole domain and a computation was terminated when the maximum sum over the three equations fell below 10^{-4}.

TABLE I

Multigrid Results for the Driven Cavity

Re	32×32	64×64	128×128
100	7	6	6
	3.0s	10.8s	47.1s
	29.4	25.1	24.7
	3.2	13.0	45.3
400	11	9	8
	4.6s	16.1s	1m 3s
	45.1	37.4	33.0
	2.9	9.4	31.2
1000	15	12	9
	6.1s	24.4s	1m 13s
	59.8	56.7	38.4
	4.5	7.6	23.8

Note. The four figures given are the number of multigrid cycles, the cpu time taken, the number of work units, and the speed-up factor over the corresponding single-grid computation.

The converged flow fields agree well with other published results [3, 6] and are discussed no further. The multigrid performance is summarized in Table I, however, where four performance measures are given for each case. These are, in order of appearance, the number of multigrid cycles required, the computing time taken, the corresponding number of work units (one work unit is the time taken for one fine grid iteration) and, for completeness, the speed-up ratio over the corresponding computation on a single grid.

Two main observations are apparent. First, the number of multigrid cycles is relatively insensitive to increasing grid density, so that computing times increase approximately linearly with grid refinement, demonstrating that optimal multigrid performance is being achieved. In fact, the number of cycles required tends to fall somewhat as the grid is refined, leading to reductions in the number of work units required, which contrasts with the results in [3] for a similar pressure correction approach, where the opposite trend is seen. The reason for this is unclear, although it may relate to differences between the methods regarding the treatment of boundaries when staggered grids are used. Second, the number of cycles required increases with increasing Reynolds number, so that computing times on a particular grid, and the number of work units required, increase by a factor up to twofold. This roughly concurs with other data for the pressure correction method [3], although the corresponding times and numbers of work units data for the coupled method (SCGS [6, 7]) show increases of up to threefold for the same range of Reynolds numbers. Few performance indicators are given for the multigrid pressure correction results in [5], and although the speed-up ratios over the corresponding single grid computations given here are similar to those in [5], these are inadequate as a true guide.

These results indicate that the multigrid method developed is robust and efficient for flow in a driven cavity. The application of a multigrid to the flow of an incompressible fluid over an obstacle in conditions of varying stability is somewhat more challenging, however. As to the flow field expected, according to linear theory (for example, Turner [20]) the flow of a stratified fluid in a bounded domain of depth D is characterized by the parameter $K = ND/\pi U$, which is the ratio of the velocity of the fastest internal gravity wave mode to the freestream velocity. The value of K is related to the Froude number via the relationship $K = D/\pi h F_h$, and the integer part of K governs the number of modes of internal gravity waves present in a steady flow, with n modes whenever $n < K \leq n + 1$. For $n = 0$ no steady lee waves are expected (their speed of propagation is lower than freestream and they are swept downstream) and all available evidence suggests that flows in this regime achieve a steady state. For $n \geq 1$, however, the flow may be unsteady, with propagation of lee waves downstream, and, since the speed of internal waves may now exceed the freestream velocity, upstream in addition. The results presented here for stratified flows over obstacles are therefore in two groups, steady and unsteady flows. The ratio of domain depth to obstacle height was kept fixed in all cases at $D/h = 5$. Steady flows were computed at conditions given by $K = 0$ ($F_h = \infty$, neutral flow), $K = 0.5$ ($F_h = 3.180$), $K = 0.8$ ($F_h = 1.989$), and $K = 1.0$ ($F_h = 1.592$), while the unsteady cases were computed at $K = 1.5$ ($F_h = 1.061$). The value $K = 1.0$ represents the transition to the unsteady regime.

Convergence in these computations was monitored in the same way as for the driven cavity, with termination when the maximum sum over the three (or four) equations fell below 10^{-4}. In the unsteady cases this criterion marked convergence for an individual timestep. Results for the steady computations were obtained for three grids covering $-20 \leq x/h \leq 60$ and $0 \leq z/h \leq 5$, the cells in each numbering 80×20, 160×40, and 320×80. The coarsest grid used in all computations was 20×5, allowing the use of a maximum of three, four, or five grid levels respectively. The grids are nonuniform, with the minimum horizontal spacing on the finest grid for both obstacles being 0.05h. For the barrier, the vertical spacing around the tip is $0.05h$, while for the cosine-shaped hill the vertical spacing at the surface is $0.025h$ (but due to the staggering the first grid point above the surface is at $z/h = 0.0125$). All multigrid computations are for fixed W-cycles, starting from an initial condition of uniform flow. The numbers of iterations in the different parts of the multigrid cycle are kept fixed in all cases, with 1 presmoothing iteration, 2 postsmoothing iterations, and 10 iterations to solve the equations on the coarsest grid. For the stratified cases on the finer grids, each computation was initialized with 10 fine grid iterations to allow partial development of the flow field, without which a typical computation would quickly diverge. Ranges of the under-relaxation parameters for all computations were 0.4–0.8, 0.25–0.4, and 0.8–0.95 for the momentum equations, the pressure correction step, and the density equation respectively, with the values required decreasing in general as the grid density, the Reynolds number, and the stratification increased. The computing times given are for double-precision arithmetic on a Silicon Graphics Indy workstation. Single grid results were computed where possible to provide meaningful speed-up factors. The single grid computations were optimised in terms of the under-relaxation parameters, and were run with a block correction routine applied to the pressures. This considerably enhanced the single grid results, but did not gain anything, and was not used, in the multigrid computations.

Steady Flows

Results are presented first for the vertical barrier with Re = 50. This Reynolds number was originally chosen [12] because the separation length in neutral flow roughly matches that seen in high Reynolds number experiments. Streamlines for the four cases computed are shown in Fig. 5, where a reduction in the length of the separated region as K increases is seen as the flow responds to the increasing vertical restoring force. A lee wave is clearly visible when $K = 1$ (Fig. 5d), for which case disturbance upstream is evident in the displacement of streamlines compared with the computations at lower values of K. The convergence performance of the multigrid scheme is given in Table II. The number of cycles required at all levels of stratification tends to fall slightly with grid refinement, and hence computing times increase approximately linearly, demonstrating that convergence rates are being achieved which are independent of the grid size used, for both neutral and stably stratified flow. As a consequence this leads to significant gains in computing time over the single grid computations (a factor of approximately 30 on the finest grid). The number of work units required is generally greater than for the driven cavity problem, but this might be expected, given the nonuniformity in the grid, the unidirectionality of the flow, and the more complicated boundary conditions. The number of work units falls with grid refinement, as a consequence of the fall in the number of cycles, but rises with increasing stratification, reflecting the increasing coupling in the equations.

The corresponding streamlines for laminar flow over the cosine obstacle at Re = 100 are shown in Fig. 6, where features similar to those seen in the flow over the barrier are evident, with the addition of a horizontal boundary layer. The length of the separated flow decreases, with separation being almost completely inhibited when $K = 1$. Upstream disturbance at this value is again evident, with the boundary layer noticeably thicker. The downstream

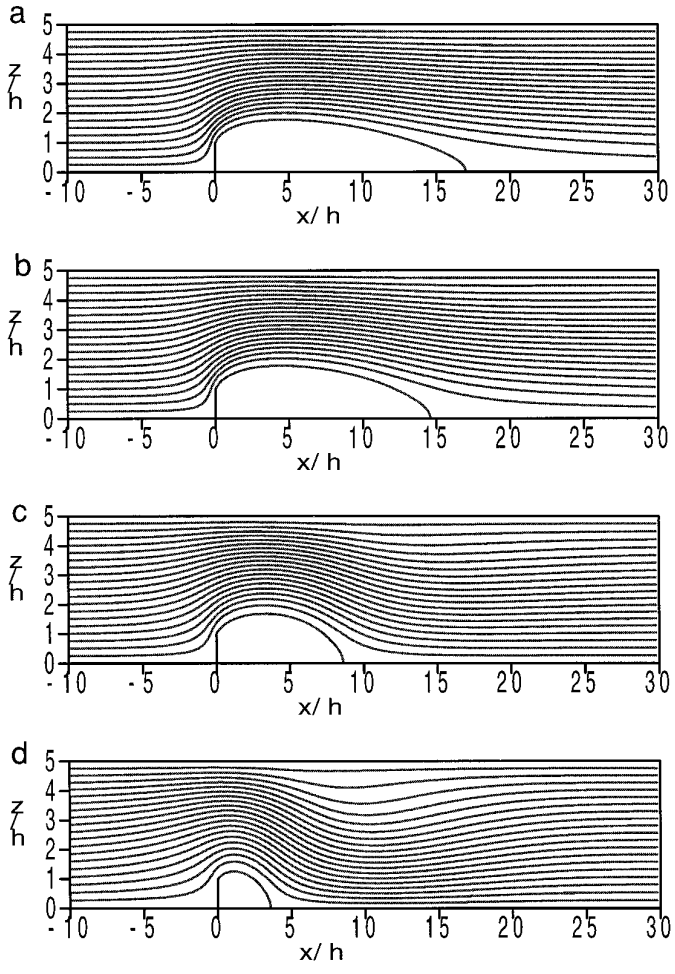

FIG. 5. Flow over the vertical barrier, Re = 50. (a) $F_h = \infty$, $K = 0$ (neutral flow); (b) $F_h = 3.180$, $K = 0.5$; (c) $F_h = 1.989$, $K = 0.8$; (d) $F_h = 1.592$, $K = 1.0$.

lee wave at this stratification is more pronounced than for the barrier, possibly because the Reynolds number is higher, but also perhaps because the boundary layer increases the apparent height of the obstacle, giving a somewhat larger effective value of K. Convergence difficulties were experienced for this case, but as mentioned above, the value $K = 1$ represents the transition to the unsteady regime, or the explanation may simply be that the discrete equations are not dissipative enough and some form of double discretisation [19] is required. (The streamlines shown and the data discussed later are generated from the results of the corresponding single grid computation, which converged satisfactorily, if somewhat slowly). The multigrid performance is shown in Table III, where computing times per cycle are now around 40% greater than for the barrier due to the inclusion of the coordinate transformation. The numbers of cycles required for convergence for a particular computation are only a little higher than for the barrier, despite the higher Reynolds number and the non-Cartesian grid. The numbers of work units are also correspondingly slightly higher, but show the same trends with grid refinement and increasing stratification. Convergence rates are again approximately independent of the grid size, with a speed-up factor of similar magnitude being achieved for neutral flow, but rather smaller for the stratified flows.

For the turbulent cases, a Reynolds number of 10,000 was used, which is typical of conditions in a towing tank, together with the mixing length turbulence model outlined earlier, with the mixing length parameter l_o set to 0.2. For the stratified cases the critical value for the Richardson number, Ri_c, was taken to be infinite, implying no modification of eddy viscosity with stratification. Streamlines for the high Reynolds number flows over the vertical barrier are shown in Fig. 7, which exhibit features similar to those in the laminar cases considered earlier, with minor differences. The first is that in the wake, streamlines recover their freestream elevations much more slowly than in the laminar cases. The second is that the lee wave, evident for $K = 1$ in the laminar case, is not seen here. The reason for this relates to the value of Ri_c used. Computations with small values ($Ri_c \leq 1$) lead to large amplitude lee waves, with breaking, for which no steady solution is possible. The large value of Ri_c actually used damps the solution and allows a steady state to be achieved. The multigrid performance is given in Table IV, where computing times per cycle are now around 30–40% greater than the corresponding laminar flows (Table II). The numbers of cycles required for a particular case are very similar to those for the laminar cases, and convergence rates independent of the grid are achieved, with only slightly smaller speed-up

TABLE II

Multigrid Results for Flow over the Vertical Barrier, Re = 50

K	80 × 20	160 × 40	320 × 80
0.0	15	12	12
	11.9s	42.4s	3m 14s
	63.6	51.4	46.6
	2.8	9.1	28.8
0.5	18	13	12
	22.6s	1m 9s	5m 21s
	98.0	67.5	63.7
	2.9	8.1	26.2
0.8	21	16	12
	24.9s	1m 32s	5m 21s
	107.6	89.8	63.6
	3.5	9.4	35.5
1.0	16	16	13
	21.9s	1m 32s	5m 39s
	94.8	90.0	67.4
	3.5	7.8	28.0

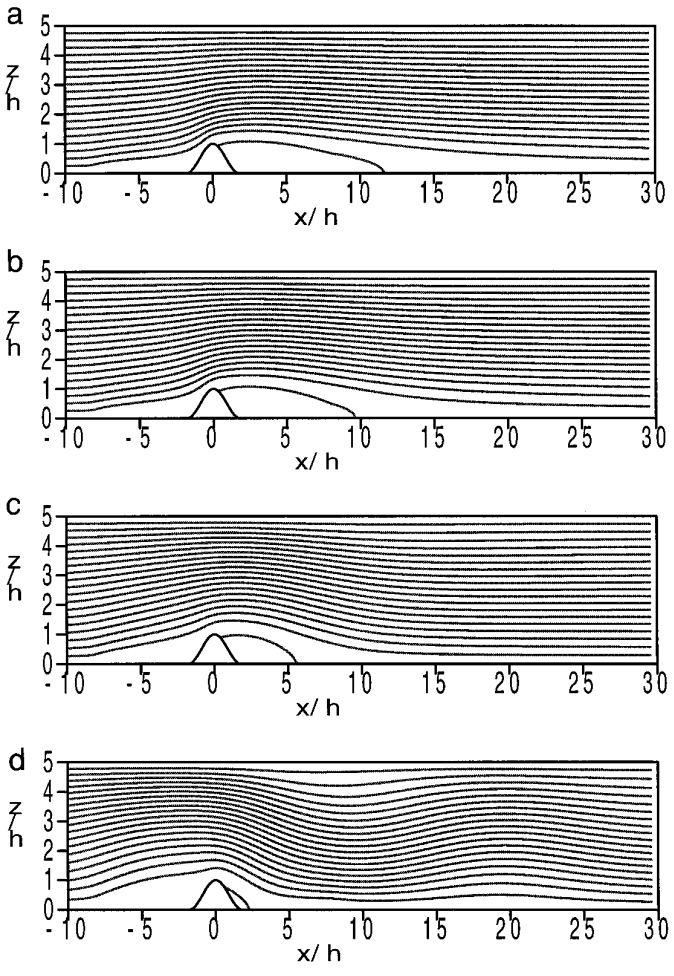

FIG. 6. Flow over the cosine obstacle, Re = 100. (a) $F_h = \infty$, $K = 0$ (neutral flow); (b) $F_h = 3.180$, $K = 0.5$; (c) $F_h = 1.989$, $K = 0.8$; (d) $F_h = 1.592$, $K = 1.0$.

factors. The number of work units for a particular case is only marginally higher than for the corresponding laminar flow.

The final set of steady computations is for high Reynolds number flow over the cosine obstacle. The streamlines are shown in Fig. 8, which show significant differences from the results of the corresponding laminar computations. The boundary layer is now much less evident, and the lengths of the recirculation regions are generally much shorter. Upstream disturbance is again evident at $K = 1$, with a very small amount of upstream separation, and the lee wave for this case is again damped out due to the parameters used in the turbulence model. The multigrid performance is given in Table V, where computing times per cycle are around 60% greater than for the corresponding laminar cases (Table III). Convergence rates are still approximately independent of the grid size, although the number of work units now is significantly greater than for the laminar cases.

Before discussing the effects of the stable density stratification on the downstream wake, some comments are appropriate regarding the dependence of the results on the grid size. In general, the recirculation zone tends to lengthen and the pressure drag rises with refinement of the grid. The overall effects in these computations are consistent with the second-order discretisation used, in that changes to such quantities fall by approximately one-quarter when the number of grid cells grid is doubled in each direction (so grid spacings are halved). No attempt was made to concentrate grid points at the downstream extent of the recirculation, and typical changes in its length on refinement to the 320 × 80 grid ranged from around 4% for long recirculation zones, in neutral flow for example, to less than 1% for the shorter recirculation zones. Changes in the corresponding values of the drag were of the same order. The exception to this was the high Reynolds number flow over the cosine obstacle, where simple grid refinement effects are complicated by the wall function treatment of the solid surface. This approach is known to be inadequate, especially for recirculating flow, and changes on grid refinement were significantly greater.

The variations in pressure drag and separation length for these four sets of results are shown in Figs. 9 and 10, where both quantities are normalised by their respective values in neutral flow. In all cases both quantities fall as K increases from zero to unity, consistent with previous data [11–13]. In three of the cases here the fall in drag (Fig. 9) is monotonic, the exception being the low Reynolds number flow over the cosine hill, where the decrease in drag at $K = 1$ due to the reduction in separation length is

TABLE III

Multigrid Results for Flow over the Cosine Obstacle, Re = 100

K	80 × 20	160 × 40	320 × 80
0.0	14	13	13
	19.5s	1m 16s	5m 17s
	74.9	66.0	58.2
	2.1	10.3	35.4
0.5	20	17	11
	35.8s	2m 29s	7m 26s
	109.2	102.9	67.5
	1.5	5.4	21.9
0.8	17	18	15
	34.7s	2m 37s	9m 45s
	106.7	111.3	84.1
	3.4	5.6	18.1
1.0	—	—	20*
	—	—	13m 30s
	—	—	116.5
	—	—	—

Note. The asterisk indicates that a fully converged solution was not obtained—see text.

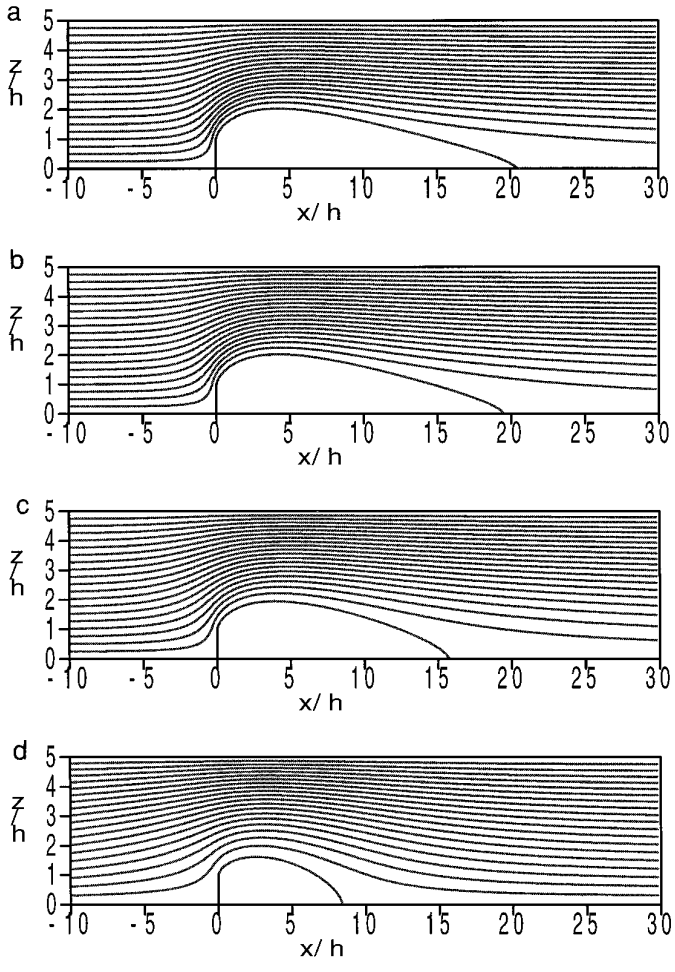

FIG. 7. Flow over the vertical barrier, Re = 10000. (a) $F_h = \infty$, $K = 0$ (neutral flow); (b) $F_h = 3.180$, $K = 0.5$; (c) $F_h = 1.989$, $K = 0.8$; (d) $F_h = 1.592$, $K = 1.0$.

presumably more than offset by the wave drag associated with the lee wave visible in the streamlines (Fig. 6d). The fall in separation length (Fig. 10) is also monotonic for three cases, the exception being the high Reynolds number flow over the cosine hill, where the separation length first increases before decreasing at $K = 1$.

Summarizing the multigrid data for the steady flows, it is clear that computing times with the multigrid algorithm are increasing approximately linearly with increasing grid size for both neutral flow and stably stratified flow, leading to significant reductions in computing time required on the finest grids. Although the greatest reductions are for the laminar flows, significant reductions are being achieved for the high Reynolds number flows as well, particularly in the case of the vertical barrier. Computing times could be reduced further by the use of a full multigrid (see [19]), where computations are initialised on the coarsest grid, and a partially converged solution is interpolated to provide the initial condition on the next finer grid in the sequence, and so on, until the finest grid is reached, when the usual multigrid algorithm can proceed starting from a good initial approximation. This technique cannot be used in the context of an unsteady flow, however, and it is to this that we now turn.

Unsteady Flows

Many phenomena of interest in meteorological flows are only elucidated by including time-dependence. Here we give a brief indication of what might be expected from the multigrid algorithm when implemented in the context of an unsteady flow. For this we consider the time-dependent flow over the vertical barrier at $K = 1.5$ ($F_h = 1.061$), in laminar (Re = 50) and turbulent (Re = 10000) conditions. Propagation of disturbances both upstream and downstream can now occur, and the computational grid was extended in both directions to cover $-100 \le x/h \le 100$, and the dimensions of the three grids used increased to 100×20, 200×40, and 400×80. According to linear theory, upstream reflections are due back in the neighbourhood of the barrier at a nondimensional time of $Ut/h = 240$. Computations were performed up to a nondimensional time of $Ut/h = 200$ on the three grids at both Reynolds numbers, and using four time steps, namely $U\,\Delta t/\mathrm{h} = 4.0, 2.0, 1.0$, and 0.5. For the high Reynolds number computations $l_o = 0.1$ and $\mathrm{Ri_c} = 0.25$.

The flow in a channel for values of K greater than unity is characterized by a periodic oscillation, first demonstrated experimentally [11] and subsequently verified numerically with the inviscid [21, 22] and viscous [13] equations. Rottman *et al.* [22] explain the oscillation in terms of a wave mode with stationary group velocity (with respect to the

TABLE IV

Multigrid Results for Flow over the Vertical Barrier, Re = 10000

K	80×20	160×40	320×80
0.0	14	13	11
	19.0s	1m 12s	4m 23s
	72.5	63.9	47.6
	2.4	5.7	26.2
0.5	15	15	12
	27.0s	1m 50s	7m 03s
	84.4	65.7	65.6
	3.0	5.3	21.3
0.8	15	16	13
	27.0s	1m 57s	7m 44s
	84.7	85.4	72.0
	3.2	6.1	24.4
1.0	—	—	18
	—	—	10m 24s
	—	—	96.8
	—	—	—

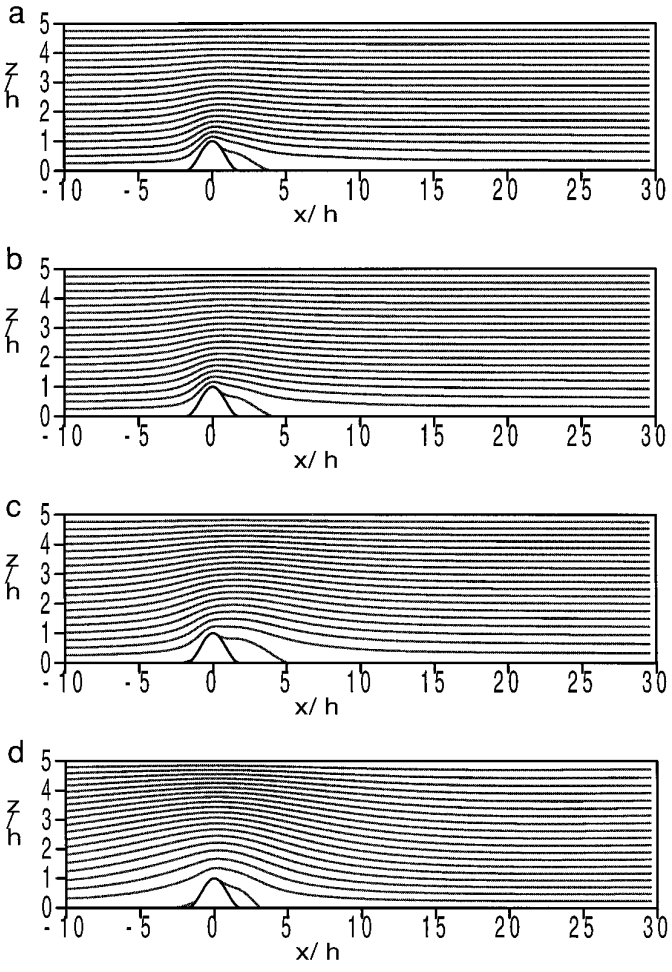

FIG. 8. Flow over the cosine obstacle, Re = 10000. (a) $F_h = \infty$, $K = 0$ (neutral flow); (b) $F_h = 3.180$, $K = 0.5$; (c) $F_h = 1.989$, $K = 0.8$; (d) $F_h = 1.592$, $K = 1.0$.

obstacle), and derived a formula for the oscillation period closely matching that observed in the experiments and numerical simulations. The amplitude of the oscillation increases with Reynolds number, and while at Re = 50 it is somewhat small, at higher Reynolds numbers it becomes very significant. The normalized drag for the flow at Re = 10000 is shown in Fig. 11 and as the values at the maxima imply, the actual drag may be far in excess of its corresponding value in neutral flow, because of the large contribution due to wave drag. The oscillation in drag is in phase with the oscillating amplitude of the wave mode over the obstacle, which is illustrated in Fig. 12, where instantaneous streamlines are shown at the high and low drag states respectively. Wave breaking occurs in the wave troughs and is clearly visible in the second trough in Fig. 12b.

The trends, in terms of the convergence characteristics, were anticipated in the Introduction. At each timestep the low frequency information in the flow is already present, and a set of small changes of high frequency are sought. Smoothing the already smooth low frequencies on coarse grids is not expected to help. Furthermore, because the frequency of the information sought increases with decreasing timestep, the multigrid performance is expected to degrade as the timestep falls. This is illustrated in Table VI for typical timesteps in the unsteady flow over the vertical barrier at Re = 50. For a particular size of timestep, convergence rates which are approximately grid-independent are being achieved as before, and the number of work units remains approximately constant. The amount of work required decreases as the timestep falls, as expected, but the advantage over a single grid computation also decreases, and in all cases is now very much less than in the

TABLE V

Multigrid Results for Flow over the Cosine Obstacle, Re = 10000

K	80 × 20	160 × 40	320 × 80
0.0	18	16	18
	45.2s	2m 44s	12m 25s
	109.6	92.7	85.3
	1.8	4.8	17.7
0.5	21	21	20
	1m 6s	4m 33s	19m 27s
	133.2	129.8	105.6
	1.6	3.0	8.6
0.8	19	21	25
	1m 0s	4m 33s	26m 34s
	121.4	129.1	142.8
	2.6	5.2	16.4
1.0	—	—	33
	—	—	37m 5s
	—	—	233.0
	—	—	—

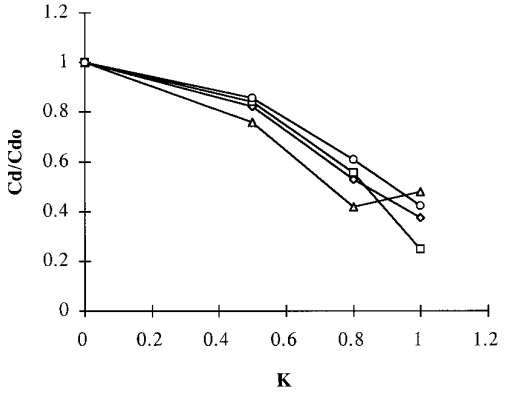

FIG. 9. Normalised drag: (Vertical barrier) ◇, Re = 50; □, Re = 10000; (Cosine obstacle) △, Re = 100; ○, Re = 10000.

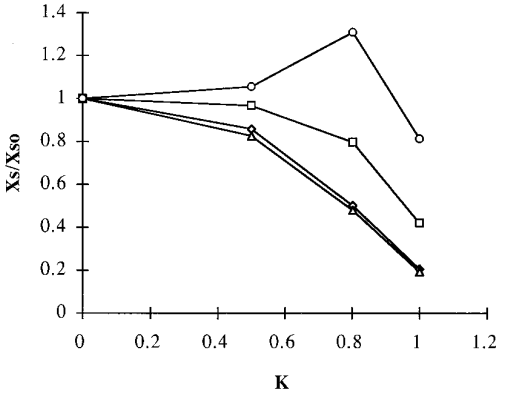

FIG. 10. Normalized separation length: (Vertical barrier) ◇, Re = 50; □, Re = 10000; (Cosine obstacle) △, Re = 100; ○, Re = 10000.

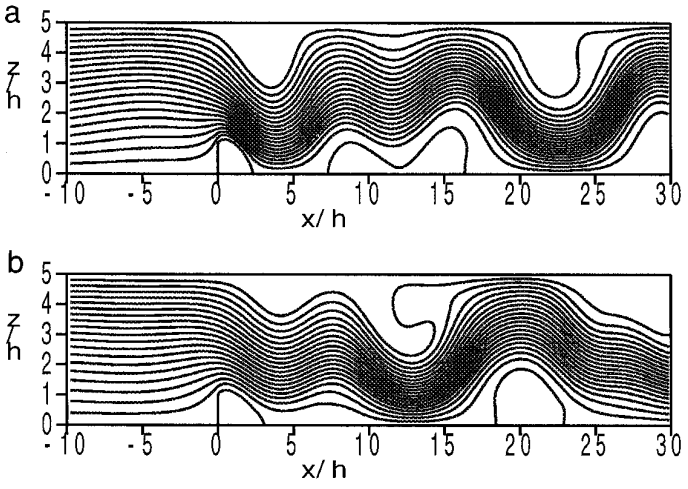

FIG. 12. Instantaneous streamlines for unsteady flow over the vertical barrier, Re = 10000, F_h = 1.062, K = 1.5. (a) High drag state, Ut/h = 125; (b) low drag state, Ut/h = 150.

corresponding steady computations (Table II). Table VII gives the results for Re = 10000, where a similar pattern is seen, with rather lower speed-up factors. These results suggest that to gain the maximum advantage from the multigrid algorithm in an unsteady computation, a high-order timestepping scheme should be chosen to allow the use of the maximum timestep permitted by accuracy considerations.

6. CONCLUSIONS

In this paper we have presented a robust multigrid method for the efficient solution of the incompressible Navier–Stokes equations with appropriate extensions for dealing with inhomogeneous flow. It has been demonstrated for the test problem of steady flow in a driven cavity and steady viscous flow over obstacles in a bounded domain under conditions of neutral stability and stable density stratification. For the two obstacle shapes used, results have been given for laminar flows at low Reynolds numbers and turbulent flows at a high Reynolds number, when a simple mixing length turbulence model was included. The results indicate that in all the cases tried convergence rates are achieved which are approximately independent of the grid size used, leading to large gains in computing time for the finest grids used. The gains obtained for the stratified cases are of the same order as those obtained in conditions of neutral flow. The gains generally decrease with Reynolds number, as expected, but are still significant for the high Reynolds number computations, especially for the vertical barrier.

Results have also been presented for unsteady flow over the vertical barrier at low and high Reynolds number in conditions of strong static stability. The multigrid algorithm was used to compute the flow at each timestep and the results indicate that although the gains in computing

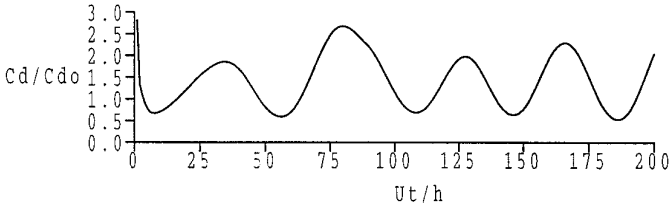

FIG. 11. Normalised drag for unsteady flow over the vertical barrier: Re = 10000, F_h = 1.062, K = 1.5.

TABLE VI

Multigrid Results for a Typical Timestep in the Computation of Unsteady Flow over the Vertical Barrier, Re = 50

$U\,\Delta t/h$	100 × 20	200 × 40	400 × 80
4.0	11	10	12
	14.0s	1m 7s	5m 47s
	42.6	48.0	46.7
	1.3	2.2	7.2
2.0	9	8	8
	11.8s	54.2s	3m 56s
	35.4	38.3	36.3
	1.1	1.8	6.7
1.0	8	8	8
	10.6s	54.2s	3m 56s
	30.3	37.3	31.8
	1.0	1.1	4.6
0.5	7	7	6
	9.4s	47.8s	3m 0s
	26.6	32.7	27.3
	1.1	1.2	3.4

TABLE VII

Multigrid Results for a Typical Timestep in the Computation of Unsteady Flow over the Vertical Barrier, Re = 10000

$U\,\Delta t/h$	100×20	200×40	400×80
4.0	13	14	26
	25.0s	2m 5s	16m 43s
	56.6	67.1	119.8
	1.6	2.1	3.9
2.0	12	11	16
	21.4s	1m 42s	10m 22s
	47.6	54.2	73.7
	1.2	2.0	3.7
1.0	9	10	13
	17.8s	1m 33s	9m 34s
	38.4	48.9	67.8
	1.0	1.5	2.5
0.5	7	8	11
	14.1s	1m 15s	7m 11s
	30.1	39.3	50.8
	1.2	1.4	3.0

time are much reduced, significant savings can still be made, even at high Reynolds numbers. Although further work appears necessary to exploit the advantages of the multigrid for time-dependent problems to the full, the study of unsteady phenomena in stratified flow over two-dimensional obstacles could be undertaken in anticipation of a significant reduction in computing time. Extension to allow the multigrid computation of flows over three-dimensional obstacles could also be carried out. Grid sizes in three dimensions are necessarily smaller in each direction, however, and gains in computing time are known to be less (see [5], for example), but should still be worthwhile.

All the results reported here were obtained with the SIMPLE pressure correction algorithm as the smoother in the multigrid algorithm. The question of which approach, coupled or uncoupled, is most advantageous for a particular flow geometry is still open, however. Work is currently in progress using a coupled method to enable an objective comparison to be made, at least for the kinds of flows considered here.

REFERENCES

1. S. V. Patankar, A calculation procedure for two-dimensional elliptic situations, *Numer. Heat Transfer* **4,** 409 (1981).
2. G. J. Shaw and S. Sivaloganathan, On the smoothing properties of the SIMPLE pressure correction algorithm, *Int. J. Numer. Methods Fluids* **8,** 441 (1988).
3. S. Sivaloganathan and G. J. Shaw, A multigrid method for recirculating flows, *Int. J. Numer. Methods Fluids* **8,** 417 (1988).
4. F. S. Lien and M. A. Leschziner, Multigrid convergence acceleration for complex flow including turbulence, in *Multigrid Methods III* (Birkhauser, Basel, 1991), p. 277.
5. F. S. Lien and M. A. Leschziner. Multigrid acceleration for turbulent flow with a nonorthogonal collacated scheme, *Comp. Meth. Appl. Mech. Engrg.* **118,** 351 (1994).
6. S. P. Vanka. Block implicit multigrid solution of Navier–Stokes equations in primitive variables. *J. Comput. Phys.* **65,** 138 (1986).
7. S. Sivaloganathan, G. J. Shaw, T. M. Shah, and D. F. Mayers. A comparison of multigrid methods for the incompressible Navier–Stokes equations, in *Numerical Methods for Fluid Dynamics,* edited by K. W. Morton and M. J. Baines, (Oxford Univ. Press, Oxford, 1988), p. 401.
8. C. H. Arakawa, A. O. Demuren, W. Rodi, and B. Schonung, Application of multigrid methods for the coupled and decoupled solution of the incompressible Navier–Stokes equations, *Notes Numer. Fluid Dynamics* **20,** 1 (1988).
9. S. Murata, N. Satofuka, and T. Kushiyama, Parabolic multigrid method for incompressible viscous flaws using a group explicit relaxation scheme, *Comp. Fluids* **19,** 33 (1991).
10. P. Wesseling, *An Introduction to Multigrid Methods* (Wiley, New York, 1991).
11. I. P. Castro, W. H. Snyder, and P. G. Baines. Obstacle drag in stratified flow, *Proc. R. Soc. London A* **429,** 119 (1990).
12. I. P. Castro. Effects of stratification on separated wakes. I. Weak static stability, in *Waves & Turbulence in Stably Stratified Flows,* edited by Mobbs & King (Oxford Univ. Press, Oxford, 1993), p. 323.
13. M. F. Paisley, I. P. Castro, and N. J. Rockliff, Steady and unsteady computations of strongly stratified flow over a vertical barrier, in *Stably Stratified Flows: Flow and Dispersion over Topography,* edited by Castro & Rockliff (Clarendon Press, Oxford, 1994), p. 39.
14. M. F. Paisley & I. P. Castro, A numerical study of wave-breaking in stratified flow over obstacles, *Dynam. Atmos. Oceans* **23,** 309 (1996).
15. P. J. Mason & R. I. Sykes, A two-dimensional numerical study of horizontal roll vortices in an inversion capped planetary boundary layer, *Quart. J. R. Met. Soc.* **108,** 801 (1982).
16. B. Van Leer, Towards the ultimate conservative difference scheme. II. Monotonicity and conservation combined in a second order scheme, *J. Comput. Phys.* **14,** 361 (1974).
17. B. P. Leonard and S. Mokhtari. Beyond first-order upwinding: the ultra-sharp alternative for non-oscillatory steady state simulation of convection. *Int. J. Numer. Methods Eng.,* **30,** 729 (1990).
18. D. D. Apsley, *Numerical Modelling of Neutral and Stably Stratified Flow and Dispersion in Complex Terrain,* Ph.D. thesis (Department of Mechanical Engineering, University of Surrey, 1995).
19. A. Brandt, *Guide to Multigrid Development,* Lecture Notes in Mathematics, Vol. 960, (Springer-Verlag, New York/Berlin, 1981).
20. J. S. Turner, *Bouyancy Effects in Fluids* (Cambridge Univ. Press, Cambridge, 1973).
21. K. G. Lamb, Numerical simulations of stratified inviscid flow over a smooth obstacle, *J. Fluid Mech.* **260,** 1 (1994).
22. J. W. Rottman, D. Broutman, and R. Grimshaw. Numerical simulations of uniformly-stratified fluid flow over topography, *J. Fluid Mech.* **306,** 1 (1996).